ACS APPLIED MATERIALS & INTERFACES

Research Article

www.acsami.org

α-Fe_2O_3 Nanoparticle-Loaded Carbon Nanofibers as Stable and High-Capacity Anodes for Rechargeable Lithium-Ion Batteries

Liwen Ji,[†] Ozan Toprakci,[†] Mataz Alcoutlabi,[†] Yingfang Yao, Ying Li, Shu Zhang, Bingkun Guo, Zhan Lin, and Xiangwu Zhang*

Fiber and Polymer Science Program, Department of Textile Engineering, Chemistry and Science, North Carolina State University, Raleigh, North Carolina 27695-8301, United States

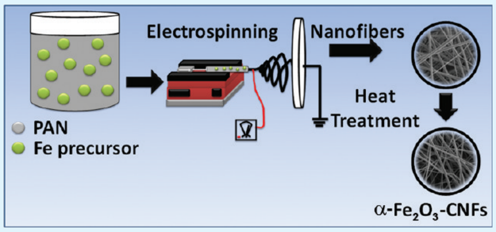

ABSTRACT: α-Fe_2O_3 nanoparticle-loaded carbon nanofiber composites were fabricated via electrospinning $FeCl_3\cdot 6H_2O$ salt-polyacrylonitrile precursors in *N*,*N*-dimethylformamide solvent and the subsequent carbonization in inert gas. Scanning electron microscopy, transmission electron microscopy, energy dispersive X-ray spectroscopy, X-ray photoelectron spectroscopy, X-ray diffraction, and elemental analysis were used to study the morphology and composition of α-Fe_2O_3-carbon nanofiber composites. It was indicated that α-Fe_2O_3 nanoparticles with an average size of about 20 nm have a homogeneous dispersion along the carbon nanofiber surface. The resultant α-Fe_2O_3-carbon nanofiber composites were used directly as the anode material in rechargeable lithium half cells, and their electrochemical performance was evaluated. The results indicated that these α-Fe_2O_3-carbon nanofiber composites have high reversible capacity, good capacity retention, and acceptable rate capability when used as anode materials for rechargeable lithium-ion batteries.

KEYWORDS: *lithium-ion batteries, anodes, nanofibers, carbon,* α-Fe_2O_3

■ INTRODUCTION

Tremendous efforts are accelerated to develop renewable energy sources to face many economic issues related to the exponential growth in global energy consumption, rapid depletion of fossil fuels, increasing greenhouse gas emission, and upward spike in crude-oil and gasoline prices. High-performance rechargeable lithium-ion batteries can potentially enable the effective use of these renewable energy sources including solar energy, wind power, etc. In addition, rechargeable lithium-ion batteries are considered as a reliable and promising source to store energy for hybrid electric vehicles (HEV) and plug-in hybrid electric vehicles (PHEV).[1−13] Currently, graphite-based anodes, which can only provide a theoretical capacity of about 372 mAh g^{-1}, are used in most commercially available rechargeable lithium-ion batteries. Due to the low theoretical capacity, graphite electrodes can only supply relatively low energy-storage ability and they cannot meet the increasing power demands mentioned above. Therefore, the design and synthesis of new anode materials are necessary to offer the promise of high-performance lithium-ion batteries with higher efficiency, greater energy density, longer cycle life, better safety, no-toxicity, and easier state-of-charge control at lower weight, volume, and cost to meet various energy storage demands for transportations.[1−14]

Iron oxides, such as hematite (Fe_2O_3) and magnetite (Fe_3O_4), are attractive anode materials for rechargeable lithium-ion batteries because they can store six and eight Li per formula unit (i.e., $Fe_2O_3 + 6Li \leftrightarrow 3Li_2O + 2Fe$ and $Fe_3O_4 + 8Li \leftrightarrow 4Li_2O + 3Fe$) via conversion reactions, resulting in high theoretical capacities of about 1007 and 926 mAh g^{-1}, respectively.[4,7,13−23] In addition, iron oxides are also abundant, inexpensive, and environmentally friendly. However, iron oxide bulk materials often suffer from poor kinetics (e.g., poor lithium-ion or electron transport) because of their low electrical conductivity, serious hysteresis between charge and discharge potentials, and poor capacity retention during cycling caused by large volume change and unstable SEI formation, especially at high current densities.[15,23−26]

Fabricating various kinds of nanoscaled iron oxide materials and dispersing these nanostructures into carbon matrixes can potentially overcome the problems of their bulk counterparts. Here, nanoscaled iron oxide can provide high reactivity for reversible redox reactions, accommodate the large volume change caused by lithium ion insertion/extraction, and facilitate more efficient electronic/ionic diffusion.[1,2,4,8,9,14,23−36] The carbon matrix can help enhance the electrical contact of the electrodes and endure the huge stresses occurred during continuous cycling. In addition, the incorporation of Li-active nanoscaled iron oxide into the carbon matrix can reduce the initial irreversible capacity and improve the Coulombic efficiency. For example, Fe_2O_3-carbon nanofiber composite anodes were prepared by Liu et al.[28] These materials retained a large reversible capacity of around 758 mAh g^{-1} after 50 cycles at 0.2 C. Zhao et al.[21] reported results on the use of Fe_3O_4-Fe-carbon composite as anodes for lithium-ion batteries. The

Received: February 24, 2012
Accepted: April 23, 2012
Published: April 23, 2012

dx.doi.org/10.1021/am300333s | *ACS Appl. Mater. Interfaces* 2012, 4, 2672−2679

nanocomposites displayed a high reversible capacity of over 600 mAh g^{-1} at a current of 50 mA g^{-1} for up to 40 cycles. Lou et al.[29] fabricated Fe_3O_4-carbon nanorods via hydrothermal method and the subsequent carbonization process. These fabricated nanocomposites delivered a high reversible capacity of 808 mA h g^{-1} after 100 cycles. He et al.[20] also reported a Fe_3O_4-CNT nanocomposite electrode with a reversible capacity of more than 656 mAhg^{-1} even after 145 cycles. More recently, graphene was also used as the carbon matrix to fabricate graphene-Fe_3O_4[14,16] or graphene-Fe_2O_3 nanocomposites.[16] Because of the ultrahigh surface area and excellent electronic conductivity,[7,9−11,14,16] these graphene-based nanocomposites exhibited high reversible capacities along with improved cycle life and rate capability.[14,16] Hence, incorporating nanoscaled Li-active iron oxide into carbon matrixes for rechargeable lithium-ion battery electrodes has a great beneficial impact on the battery performance.[7,14−22,37]

In this work, α-Fe_2O_3 nanoparticle-loaded carbon nanofibers (α-Fe_2O_3-CNFs) were fabricated by electrospinning of $FeCl_3{\cdot}6H_2O$ salt-polyacrylonitrile (PAN) precursors and the subsequent thermal treatments. α-Fe_2O_3-CNFs exhibited enhanced surface-to-volume ratio, numerous reactive sites, facile electronic/ionic transfer, and reduced transport pathway for both electrons and Li ions when these Li-active α-Fe_2O_3-CNFs were used as anodes for rechargeable lithium-ion batteries.[1,4,28,30−36] As a result, promising electrochemical performance, such as large reversible capacity, high Coulombic efficiency, slow capacity fading after prolonged cycling, and excellent rate capacity upon increased currents, was obtained.

■ EXPERIMENTAL DETAILS

Materials, Preparations, and Characterizations. PAN was purchased from Fisher Scientific. Ferric chloride hexahydrate ($FeCl_3{\cdot}6H_2O$) and solvent *N,N*-dimethylformamide (DMF) were purchased from Aldrich. All these reagents were used without further purification. DMF solutions of PAN (8 wt %) containing different amounts of $FeCl_3{\cdot}6H_2O$ (1, 2, 5, and 15 wt %) were prepared at 60 °C with mechanical stirring for at least 48 h to obtain homogeneous dispersions. For comparison, pure PAN (8 wt %) in DMF solution was also prepared.

A variable high voltage power supply (Gamma ES40P) was used to provide a high voltage of about 14 kV for electrospinning with 0.5 mL h^{-1} flow rate and 15 cm needle-to-collector distance. The electrospun $FeCl_3{\cdot}6H_2O$-PAN bicomponent nanofibers were first stabilized in an air environment at 280 °C for 6 h (heating rate was 5 °C min^{-1}) and then carbonized in argon atmosphere at 600 °C for 8 h (heating rate was 2 °C min^{-1}).

The morphology and diameter of $FeCl_3{\cdot}6H_2O$-PAN bicomponent nanofibers and their carbonized products (α-Fe_2O_3-CNFs) were characterized using scanning electron microscopy (JEOL 6400F Field Emission SEM at 5 kV) and transmission electron microscopy (Hitachi HF-2000 TEM at 200 kV). Energy dispersive X-ray spectroscopy (EDS, Hitachi S-3200N at 1 kV) was performed to measure the composition of the composite nanofibers. X-ray photoelectron spectroscopy (XPS) was also used to measure elemental compositions and chemical states. The structural variations were identified by wide-angle X-ray diffraction (WAXD, Philips X'Pert PRO MRD HR X-ray Diffraction System, Cu Kα, λ = 1.5405 Å) and Raman spectroscopy (Horiba Jobin Yvon LabRam Aramis Microscope, 633 nm He Ne Laser).

Electrochemical Performance Evaluation. The electrochemical performance was evaluated using 2032 coin-type cells (Hohsen Corp.). The α-Fe_2O_3-CNF electrodes have an average thickness of 40 μm, a weight of around 2 mg, and a diameter of about 12 mm, and they were attached onto copper foils. Lithium ribbon (0.38 mm thick, Aldrich) was used as the counter electrode. Separion S240 P25 (Degussa AG, 25 μm) was used as the separator. The electrolyte used was 1 M lithium hexafluorophosphate ($LiPF_6$), dissolved in 1/1 (v/v) ethylene carbonate (EC)/ethyl methyl carbonate (EMC) (Ferro Corp.). Cells were assembled in a high-purity argon-filled glovebox. Cyclic voltammetry (CV) measurements were performed using Gamry reference 600 Potentiostat at 0.05 mV s^{-1} scan rate between 0.05 and 2.80 V. Charge (lithium insertion) and discharge (lithium extraction) were conducted using an Arbin automatic battery cycler at several different current densities between cutoff potentials of 0.05 and 2.80 V. The capacities were calculated on the basis of the weight of α-Fe_2O_3-CNFs. Finally, the surface morphologies of α-Fe_2O_3-CNF anodes after 75 charge/discharge cycles were examined using JEOL 6400F FESEM at 5 kV.

■ RESULTS AND DISCUSSION

Morphological Properties of $FeCl_3{\cdot}6H_2O$-PAN and α-Fe_2O_3-CNF Composites. Figure 1 shows SEM images of pure PAN and $FeCl_3{\cdot}6H_2O$-PAN precursor nanofibers with different $FeCl_3{\cdot}6H_2O$ concentrations. All electrospun PAN and $FeCl_3{\cdot}6H_2O$-PAN nanofibers are straight and exhibit homogeneously distributed diameters. The fiber diameter increases with the increase of $FeCl_3{\cdot}6H_2O$ concentration because of the increased solution viscosity at high salt concentration.[33] For example, the average diameters of electrospun $FeCl_3{\cdot}6H_2O$-PAN nanofibers at different $FeCl_3{\cdot}6H_2O$ concentrations of 0 (pure PAN), 1, 2, 5, and 15 wt % are 250, 325, 375, 435, and 635 nm, respectively. In addition, with the increase in $FeCl_3{\cdot}6H_2O$ concentration, the surface becomes rougher and some undulating structures and even pores appear (Figure 1h,j).

Electrospun pure PAN and $FeCl_3{\cdot}6H_2O$-PAN nanofibers with different $FeCl_3{\cdot}6H_2O$ concentrations of 0, 1, 2, 5, and 15 wt % were stabilized in an air environment at 280 °C, followed by carbonization in argon atmosphere at 600 °C for 8 h. SEM images of the resultant CNFs and α-Fe_2O_3-CNFs are shown in Figure 2. It is seen that the fiber morphologies of α-Fe_2O_3-CNFs are similar with that of the corresponding $FeCl_3{\cdot}6H_2O$-PAN precursors (Figure 1). However, the average fiber diameters become smaller because of the weight loss resulting from the removal of various components during the carbonization process. The average diameters of α-Fe_2O_3-CNFs, with different $FeCl_3{\cdot}6H_2O$ concentrations of 0, 1, 2, 5, and 15 wt % in precursors, were calculated and were found to be approximately 175, 193, 212, 298, and 487 nm, respectively.

Figure 3 shows TEM images of electrospun 15 wt % $FeCl_3{\cdot}6H_2O$-PAN nanofibers (Figure 3a,b) and the corresponding α-Fe_2O_3-CNF composites (Figure 3c−f). As shown in Figure 3a,b, electrospun 15 wt % $FeCl_3{\cdot}6H_2O$-PAN nanofibers exhibit rough surface morphology. After carbonization, the presence of α-Fe_2O_3 nanoparticles with clearly spherical morphology and an average size of about 20 nm can be clearly seen in the carbonized product (Figure 3c−f). From Figure 3c−f, it is also seen that some of the α-Fe_2O_3 nanoparticles are embedded inside the fiber and have uniform dispersion along the fiber direction.

Figure 4 shows EDS spectra of CNFs and α-Fe_2O_3-CNFs with different α-Fe_2O_3 contents in the precursors. The existence of iron and oxygen elements within the carbonized composite nanofibers is confirmed. It is also seen that the Fe peaks become more intense when $FeCl_3{\cdot}6H_2O$ concentration increases from 1 to 15 wt %. Elemental analysis was also conducted to calculate the amount of α-Fe_2O_3 nanoparticles in α-Fe_2O_3-CNFs, and it was found that the content of α-Fe_2O_3 nanoparticles was around 0.54, 1.17, 2.28, and 11.33 wt % for

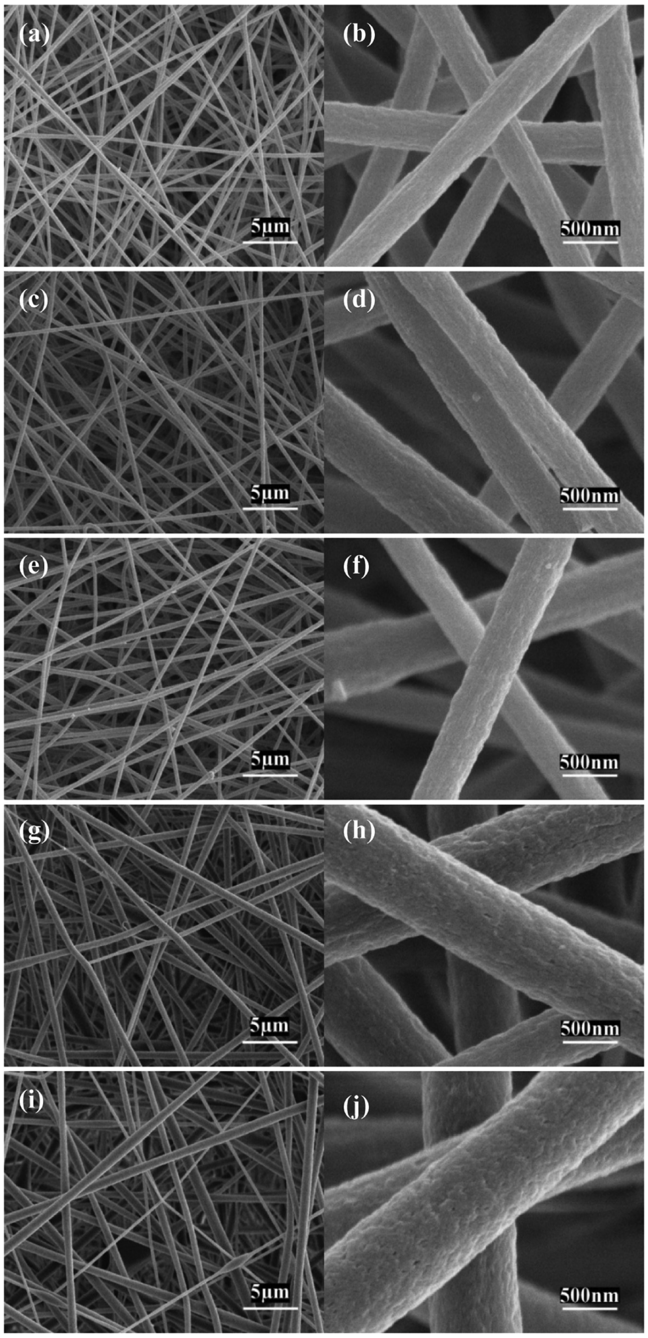

Figure 1. SEM images of $FeCl_3 \cdot 6H_2O$-PAN bicomponent nanofibers with different $FeCl_3 \cdot 6H_2O$ concentrations: (a, b) 0, (c, d) 1, (e, f) 2, (g, h) 5, and (i, j) 15 wt %.

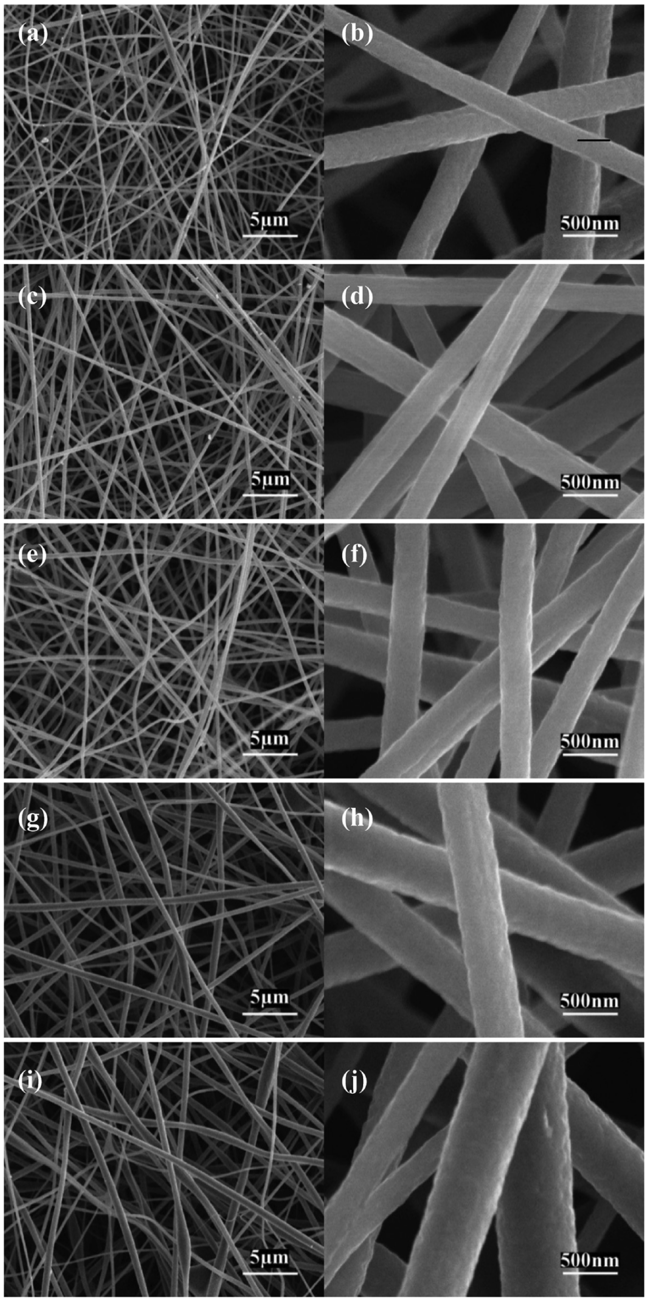

Figure 2. SEM images of α-Fe_2O_3-CNFs prepared from $FeCl_3 \cdot 6H_2O$-PAN precursors with different $FeCl_3 \cdot 6H_2O$ concentrations: (a, b) 0, (c, d) 1, (e, f) 2, (g, h) 5, and (i, j) 15 wt %.

α-Fe_2O_3-CNFs prepared from 1, 2, 5, and 15 wt % $FeCl_3 \cdot 6H_2O$-PAN precursors, respectively.

Structural Properties of α-Fe_2O_3-CNF Composites. The crystallinity and phase composition of CNFs and α-Fe_2O_3-CNFs with different α-Fe_2O_3 contents were investigated using a WAXD. The results are shown in Figure 5A, where the broad diffraction peak at around 2θ of 25° (002) confirms the disordered structure for the CNF matrix.[36,34] However, the X-ray diffraction analysis (XRD) curves in Figure 5A do not show any α-Fe_2O_3 peaks, and this may be caused by the small content of α-Fe_2O_3 or by its amorphous nature in the as-prepared α-Fe_2O_3-CNF composites.

Figure 5B shows the Raman spectroscopy results of CNFs and α-Fe_2O_3-CNFs with different α-Fe_2O_3 contents. All samples exhibit well-known D-band (disorder-induced phonon mode) in the range of 1250−1450 cm^{-1} and G-band (graphite band) between 1550 and 1660 cm^{-1}. The former one can be attributed to defects and disordered portions of carbon (sp^3-coordinated) whereas the later one is indicative of ordered graphitic crystallites of carbon (sp^2-coordinated).[34−36] The relative intensities (I_D/I_G) can be used to analyze the amount of carbon defects in the CNFs and α-Fe_2O_3-CNFs (Table 1). A low I_D/I_G ratio indicates the presence of a larger amount of sp^2-coordinated carbon. From Table 1, it is seen that pure CNFs contain a significant amount of disordered sections and defects and have a relatively high I_D/I_G ratio of 1.202. The I_D/I_G ratio

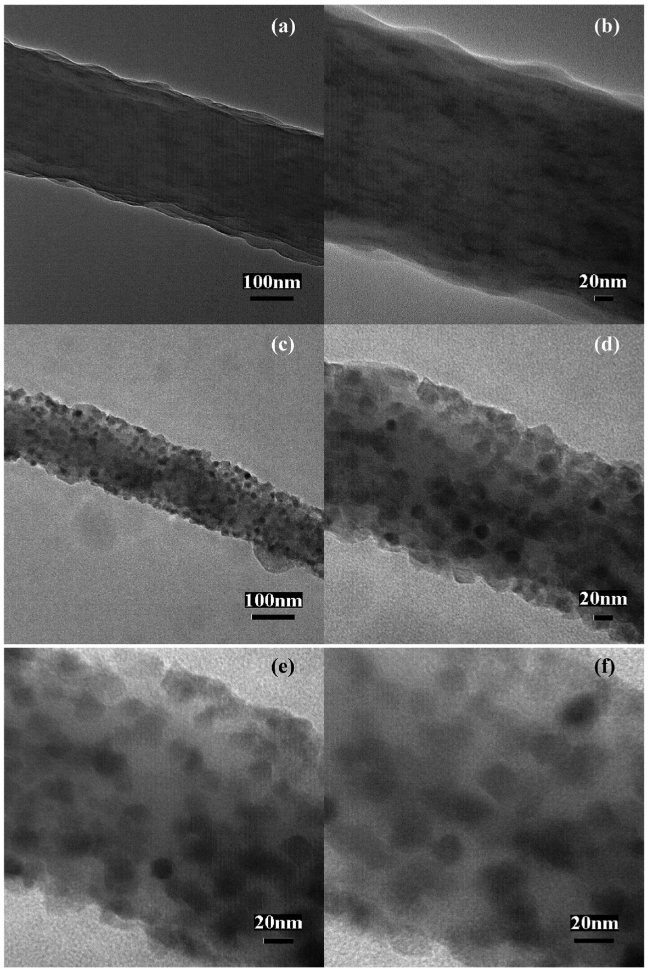

Figure 3. TEM images of (a, b) 15 wt % $FeCl_3·6H_2O$-PAN bicomponent nanofibers and (c−f) the corresponding α-Fe_2O_3-CNFs carbonized at 600 °C for 8 h.

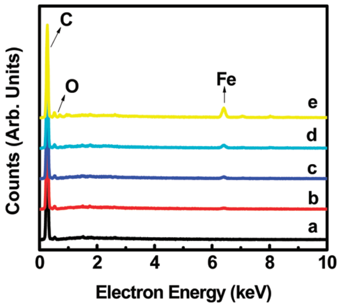

Figure 4. EDS spectra of α-Fe_2O_3-CNFs prepared from $FeCl_3·6H_2O$-PAN precursors with different $FeCl_3·6H_2O$ concentrations: (a) 0, (b) 1, (c) 2, (d) 5, and (e) 15 wt %.

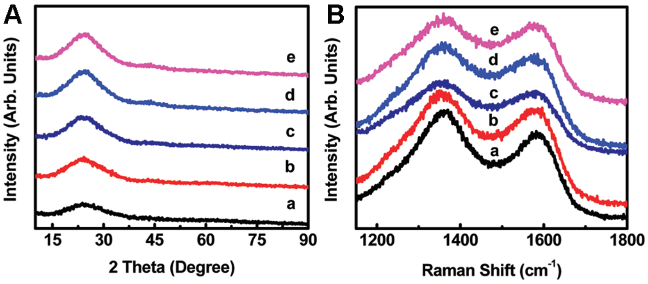

Figure 5. (A) XRD patterns and (B) Raman spectra of α-Fe_2O_3-CNFs prepared from $FeCl_3·6H_2O$-PAN precursors with different $FeCl_3·6H_2O$ concentrations: (a) 0, (b) 1, (c) 2, (d) 5, and (e) 15 wt %.

Table 1. Characteristic Raman Bands of CNFs and α-Fe_2O_3-CNFs Prepared from $FeCl_3·6H_2O$-PAN Precursors with Different $FeCl_3·6H_2O$ Concentrations[a]

sample ID	D peak (cm^{-1})	G peak (cm^{-1})	I_D/I_G value
a	1370	1582	1.202
b	1350	1596	1.132
c	1363	1581	1.131
d	1355	1585	1.092
e	1360	1566	1.088

[a] (a) 0, (b) 1, (c) 2, (d) 5, and (e) 15 wt %.

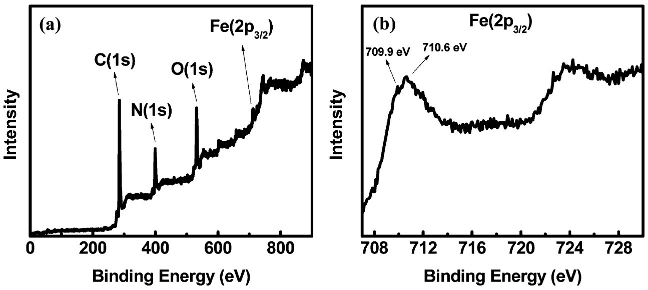

Figure 6. XPS results of α-Fe_2O_3-CNFs prepared from a 15 wt % $FeCl_3·6H_2O$-PAN precursor.

decreases from 1.202 to 1.088 as the $FeCl_3·6H_2O$ concentration increases from 0 to 15 wt % in the precursor. This indicates that the presence of $FeCl_3·6H_2O$ in the precursor helps to create more ordered carbon in the resultant CNFs.

In order to determine the surface bond state, structural defects, and chemical composition of α-Fe_2O_3-CNF composites, XPS measurements were also carried out. Figure 6 shows XPS spectra of α-Fe_2O_3-CNFs prepared from the 15 wt % $FeCl_3·6H_2O$-PAN precursor. The Fe $2p_{3/2}$ region (shown in Figure 6b) has two distinct peaks split by about 0.7 eV (709.9 and 710.6 eV) in the as-prepared α-Fe_2O_3-CNFs. In addition, the peak structures are asymmetric and the high binding energy side is found to have stronger intensity. This multiplet splitting distribution of peaks indicates the existence of α-Fe_2O_3 in the as-formed α-Fe_2O_3-CNFs.[38−41] The existence of the O 1s peak at 730.2 eV shows that there is no metallic iron (Fe^0) in the composite.[38−41]

Electrochemical Performance of α-Fe_2O_3-CNF Composites. Figure 7 shows the cyclic voltammetry (CV) curves of pure CNFs and α-Fe_2O_3-CNFs. It is seen in Figure 7a that the CNF anode prepared from pure PAN precursor exhibits a cathodic peak at about 0.3 V and two wide oxidation peaks at about 0.5 and 1.5 V, respectively. As shown in Figure 7b−e, at the first cycle, all α-Fe_2O_3-CNF anodes exhibit a clear cathodic peak at about 0.65 V where the intensity increases with increasing α-Fe_2O_3 content. The reduction peak at 0.65 V in the cathodic sweep might be related to the Li insertion into α-Fe_2O_3 to form Li_xFeO_3. The further decomposition of Li_xFeO_3 to form Fe^0 leads to the crystal structure destruction,[42] as well as the formation of the solid electrolyte interface (SEI) film.[19,26,27,43−47] In the subsequent cycles, the reduction peak at 0.65 V disappears, indicating the occurrence of some irreversible processes in the electrode material in the first cycle. For all α-Fe_2O_3-CNF anodes, a wide but unclear

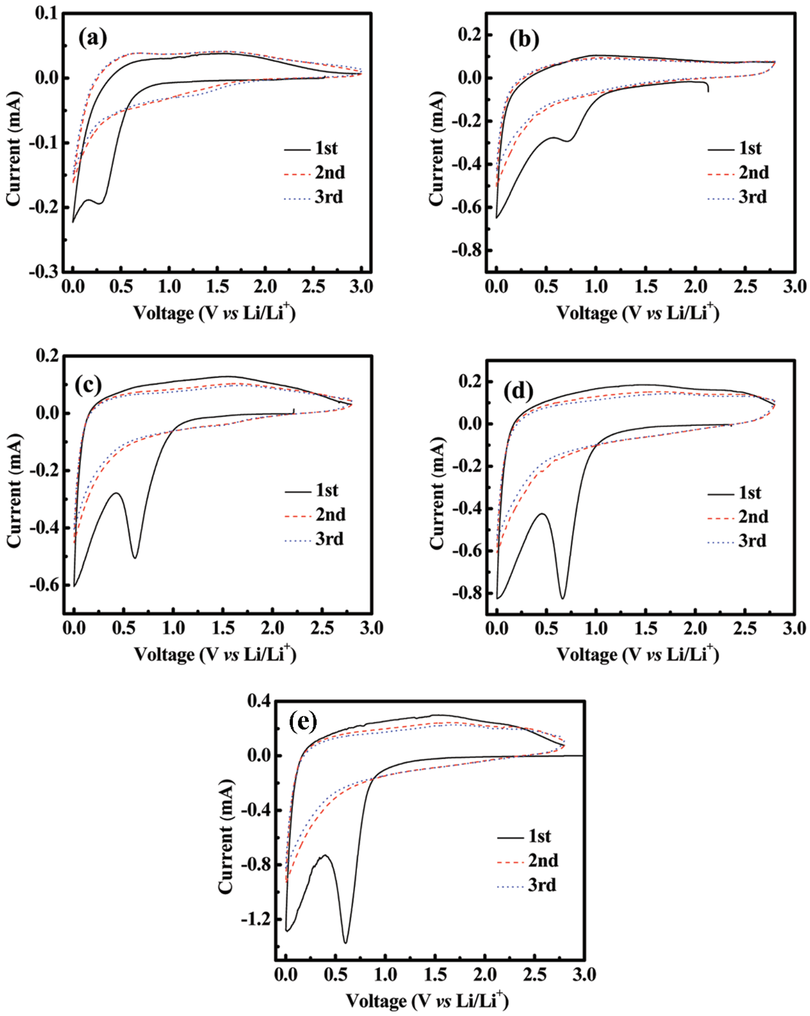

Figure 7. CV curves of α-Fe_2O_3-CNFs prepared from $FeCl_3{\cdot}6H_2O$-PAN precursors with different $FeCl_3{\cdot}6H_2O$ concentrations: (a) 0, (b) 1, (c) 2, (d) 5, and (e) 15 wt %. Scan rate: 0.05 mV s^{-1}.

oxidation peak at about 1.6 V is also recorded at the first cycle anodic process, which corresponds to the reversible oxidation from Fe^0 to Fe^{3+} (or Fe^{2+}).[26,27,43,48] All oxidation peaks are unclear after the first cycle.

It was reported that during the charge/discharge process, Fe_2O_3-based anodes have the following possible reactions:[14,20,42]

$$Fe_2O_3 + 0.6Li^+ + 0.6e^- \rightarrow Li_{0.6}Fe_2O_3 \quad \text{(theoretically at 1.1 V, typically at 1.6 V)} \tag{1}$$

$$Fe_2O_3 + 1.8Li^+ + 1.8e^- \rightarrow Li_{1.8}Fe_2O_3 \quad \text{(theoretically at 0.9 V, typically at 0.86 V)} \tag{2}$$

$$Fe_2O_3 + Li^+ + e \rightarrow Li_xFe_2O_3 \quad (x = \text{others}, \ \text{at 0.65 V}) \tag{3}$$

Among these reactions, Reaction 3 is irreversible because it is usually followed by the decomposition and destruction of the crystal structure. However, in Reaction 2, $Li_{1.8}Fe_2O_3$ can further react with Li^+ and e^- to form Fe and Li^2O by following:[42]

$$Li_{1.8}Fe_2O_3 + 4.2Li^+ + 4.2e^- \rightarrow 2Fe + 3Li_2O \tag{4}$$

The total reaction is:

$$Fe_2O_3 + 6Li^+ + 6e^- \leftrightarrow 2Fe + 3Li_2O \tag{5}$$

which is reversible.[42]

From the CV results shown in Figure 7, it is seen that the main reaction is Reaction 3 because there is a sharp reduction peak at about 0.65 V during the first cathodic scanning. Reactions 1, 2, and 4 are not apparent since there are no clear reduction peaks at 1.6 and 0.86 V. The absence of Reactions 1, 2, and 4 is the result of low α-Fe_2O_3 content in the synthesized α-Fe_2O_3-CNFs nanocomposites.

Figure 8a shows typical charge (lithium insertion)/discharge (lithium extraction) curves of α-Fe_2O_3-CNFs prepared from the 15 wt % $FeCl_3{\cdot}6H_2O$-PAN precursor. The charge/discharge curves were obtained at a constant current density of 50 mA g^{-1} over a potential window of 0.05−2.8 V. It is seen in Figure 8a that the voltage steeply declines to about 0.9−1.0 V during the first charge process and then slowly decreases until a total charge capacity of 1008 mAh g^{-1} is reached. This high capacity value, which is even similar to the theoretical capacity of Fe_2O_3, can be partially assigned to the polymer surface-layer formation and the charge storage via the surface charge-transfer mechanism.[24,44,49,50] The plateau at 0.9−1.0 V may also be associated with the electrolyte decomposition, SEI formation, and the initial reduction of amorphous α-Fe_2O_3 to Fe^0 and Li_2O.[26] The corresponding first-cycle discharge profile shows a

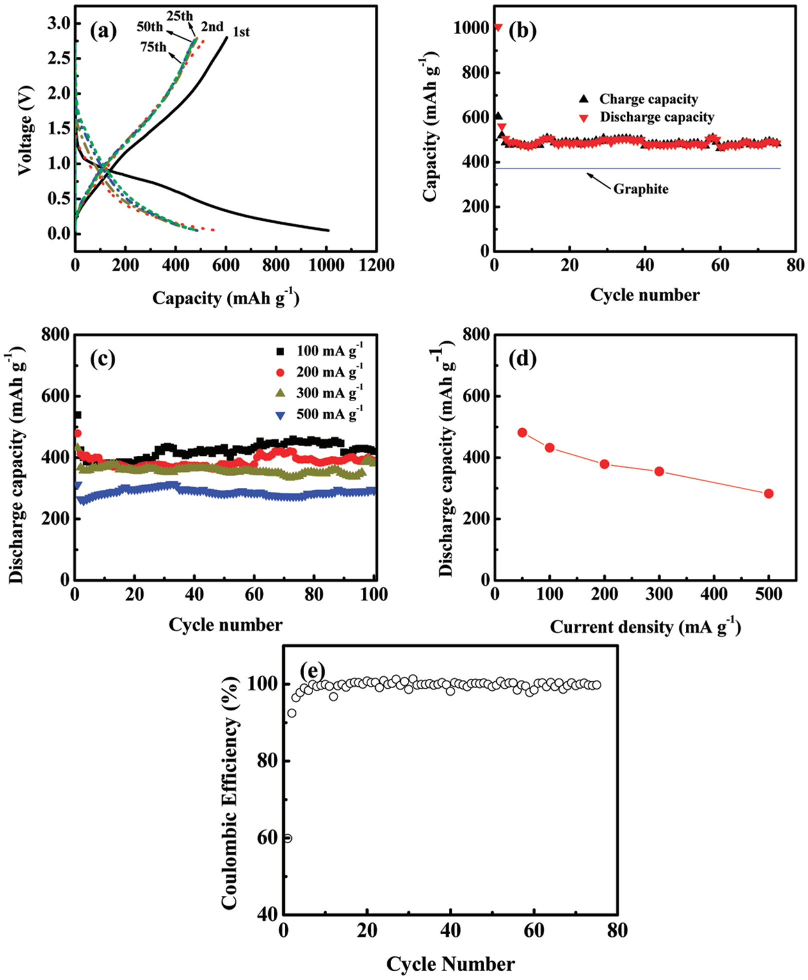

Figure 8. (a) Charge−discharge curves of α-Fe_2O_3-CNFs at 50 mA g^{-1}; (b) cycling performance of α-Fe_2O_3-CNFs at 50 mA g^{-1}; (c) cycling performance of α-Fe_2O_3-CNFs at higher current densities; (d) rate capabilities of α-Fe_2O_3-CNFs; and (e) Coulombic efficiency at 50 mA g^{-1}. The α-Fe_2O_3-CNFs were prepared from the 15 wt % $FeCl_3 \cdot 6H_2O$-PAN precursors.

Table 2. Comparison of the Electrochemical Performance of α-Fe_2O_3-CNFs with Other Reported FeO_x/Carbon Nanocomposites

materials	fabrication methods	electrochemical performance
graphene-Fe_3O_4	chemical coprecipitation	high reversible capacity of more than 900, 400, and 200 mAh g^{-1} at different current rates of 0.05, 5, and 10 C, respectively[14]
carbon-Fe_3O_4 nanospindles	reduction of α-Fe_2O_3 nanospindles with carbon coating	high reversible capacity of about 745 mAh g^{-1} at 0.2 C and 600 mA h g^{-1} at 0.5 C[15]
α-Fe_2O_3-C nanocomposite	in situ carbonization of surfactants	high reversible capacity of 688 mAh g^{-1} after 50 cycles at 0.2 C rate and 370 mAh g^{-1} after 20 cycles at 2 C[19]
CNTs-Fe_3O_4 nanocomposites	chemical coprecipitation	high discharge capacity of 661 and 656 mAh g^{-1} at the first and 145th cycles at 100 mA g^{-1}[20]
Fe_3O_4-Fe-carbon composites	sol−gel polymerization and heat-treatment process	high reversible capacity of over 600 mAh g^{-1} at a current of 50 mA g^{-1} for up to 40 cycles[21]
Fe_3O_4-carbon nanocomposites	hydrothermal reactions	stable specific capacity of 1010 mAh g^{-1} after 50 cycles at 0.1 C[22]
Fe_2O_3 nanorods-carbon nanocomposites	electrospinning and hydrothermal method	high reversible capacity of about 758 mAh g^{-1} after 50 cycles at 0.2 C[28]
Fe_3O_4-carbon nanorods	hydrothermal method and carbonization process	high reversible capacity of about 808 mAh g^{-1} after 100 cycles at 1 C[29]
graphene-Fe_2O_3	hydrothermal reaction	high reversible capacity of 660 mAh g^{-1} for up to 100 cycles at the current density of 160 mA g^{-1}[16]
α-Fe_2O_3-CNFs	electrospinning and carbonization	high reversible capacity of about 604 mAh g^{-1} at 50 mA g^{-1}, improved capacity retention for at least 100 cycles

slight polarization at around 0.75 V, followed by a smoothly increasing curve. The first-cycle discharge capacity is about 604 mAh g^{-1}, corresponding to a Coulombic efficiency of about 60%. This relatively small Coulombic efficiency can be attributed to the above-mentioned irreversible reactions, the decomposition of the electrolyte, and the formation of SEI film or the existence of other inactive materials. However, after the first cycle, the efficiency remains nearly 100%. From Figure 8a, it is also seen that the discharge capacity of the α-Fe_2O_3-CNF anode is about 519 mAh g^{-1} at the second cycle. The relatively high capacity of α-Fe_2O_3-CNFs produced from the 15 wt % $FeCl_3{\cdot}6H_2O$-PAN precursor might be due to the synergetic effects of carbon matrix and amorphous α-Fe_2O_3 nanoparticles as well as the special nanostructure of the as-prepared α-Fe_2O_3-CNF composites.

The cycling performance of α-Fe_2O_3-CNFs is shown in Figure 8b. After 75 cycles, the reversible capacities remain relatively constant at around 488 mAh g^{-1}. The capacity retention at the 75th cycle is 81%, indicating a relatively slow capacity fading. Both of the reversible capacity and capacity retention are comparable to most of the reported FeO_x@carbon nanocomposites (see Table 2 for the detailed comparison). In addition, the reversible capacity of α-Fe_2O_3-CNFs is higher than the theoretical capacity (372 mAh g^{-1}) of graphite, which is currently used in commercial rechargeable lithium-ion batteries. Figure 8e also displays that the α-Fe_2O_3-CNFs have high Coulombic efficiency of about 100% after the first charging/discharging cycle, indicating excellent reversibility. It has been widely reported that a higher amount of host carbon phase improves the cycling stability of the anode but reduces the specific capacity. The relatively good cycling performance of α-Fe_2O_3-CNFs can be ascribed to their unique composite structure, such as the increased electrode connectivity, the unique one-dimensional fiber structure, and the effective lithium ion transportation at the large nanofiber surface.

The cycling performance and second-cycle discharge capacities of α-Fe_2O_3-CNFs at different current densities of 50, 100, 200, and 500 mA g^{-1} are shown in Figure 8c,d, respectively. At a current density of 100 mA g^{-1}, the discharge capacity of α-Fe_2O_3-CNFs shows slightly larger degradation compared to that at 50 mA g^{-1}. However, a relatively small capacity decrease is observed when the current density increases from 100 to 200 mA g^{-1}. At a much higher current density of 500 mA g^{-1}, α-Fe_2O_3-CNFs exhibit an average reversible capacity of 288 mAh g^{-1}, indicating a satisfactory rate capability. The average reversible capacities of α-Fe_2O_3-CNFs composites prepared from the 15 wt % $FeCl_3{\cdot}6H_2O$-PAN precursor are obtained as 422, 387, 358, and 288 mAh g^{-1}, respectively, for current densities of 100, 200, 300, and 500 mA g^{-1}. It is worthwhile to mention here that the rate capability of α-Fe_2O_3-CNFs prepared from the 15 wt % $FeCl_3{\cdot}6H_2O$-PAN precursor is much better than that of pure CNFs and also some commercial graphite anodes.[35]

In order to understand the influence of charge/discharge process on the structural integrity of α-Fe_2O_3-CNF composites, SEM images of α-Fe_2O_3-CNFs were taken after 75 charge/discharge cycles at a constant current density of 50 mA g^{-1} (Figure 9). It is seen that the composite still maintains the nanofibrous structure after prolonged charging/discharging, which indicates that the structural integrity of the material is preserved during long-time charge/discharge cycling. This is because of the remarkable characteristics of the CNF matrix, which can withstand the large volume expansion and shrinkage during lithium insertion and extraction and preserve the integrity of the electrodes during cycling.

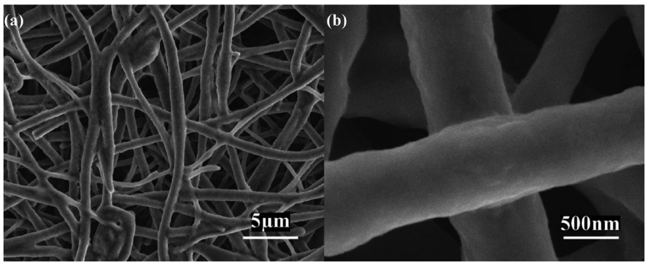

Figure 9. SEM images of α-Fe_2O_3-CNF anodes prepared from the 15 wt % $FeCl_3{\cdot}6H_2O$-PAN precursor after 75 cycles' charging/discharging at a constant current density of 50 mA g^{-1}.

The α-Fe_2O_3-CNFs show high reversible capacity, improved cyclability, and good rate capability because of their unique one-dimensional nanofibrous structure. To obtain a good electrochemical performance, electrode materials should always possess the properties of high lithium storage, fast Li insertion/release kinetics, good electronic and ionic conductivities, and appropriate mechanical strength to stabilize the Li-ion transfer pathway for Li uptake/removal. In the case of α-Fe_2O_3-CNFs, the one-dimensional fibrous structure can provide a large surface area, enhance the contact between the electrolyte and electrode, and fascinate the impregnation of the electrolyte into the electrode. This unique nanostructure can also provide continuous conducting pathways for Li^+ and e^- transports. In addition, the composite CNFs can reduce the strain/stress associated with the conversion reaction and hence can preserve the integrity of the electrode upon charge/discharge cycling. These synergic effects help α-Fe_2O_3-CNFs combine the virtues of both transition metal oxides and carbon and exhibit excellent overall electrochemical performance when used as anodes in rechargeable lithium-ion batteries.

CONCLUSIONS

Highly dispersed α-Fe_2O_3 nanoparticles with an average size of about 20 nm were successfully loaded in CNFs through cost-effective, economically viable electrospinning and thermal treatment processes. When used as binder-free anode materials for rechargeable lithium-ion batteries, these hybrid nanostructured electrodes that have interconnected nanostructures with conductive additive nanophases exhibited a high reversible capacity of about 604 mAh g^{-1} at 50 mA g^{-1}, improved capacity retention for at least 100 cycles, and enhanced rate performance even at the high current density of 500 mA g^{-1}. The good electrochemical performance of these α-Fe_2O_3-CNF composites is a result of the cooperative effects of α-Fe_2O_3 nanoparticles (excellent Li-storage capacity) and carbon matrix (high Li-storage capacity and fast Li-ion/electron diffusion), as well as the unique one-dimensional nanofiber structures with large surface area and high length−diameter ratio.

AUTHOR INFORMATION

Corresponding Author

*Tel: 919-515-6547. Fax: 919-515-6532. E-mail: xiangwu_zhang@ncsu.edu.

Author Contributions

[†]These three authors contributed equally to this work.

Notes

The authors declare no competing financial interest.

ACKNOWLEDGMENTS

This work was supported by the U.S. Department of Energy (No. DE-EE0001177), the ERC Program of the National Science Foundation under Award Number EEC-08212121, and the Advanced Transportation Energy Center at North Carolina State University.

■ REFERENCES

(1) Zhang, X.; Ji, L.; Toprakci, O.; Liang, Y.; Alcoutlabi, M. *Polym. Rev.* **2011**, *51*, 239.
(2) Liu, J.; Cao, G.; Yang, Z.; Wang, D.; Dubois, D.; Zhou, X.; Graff, G. L.; Pederson, L. R.; Zhang, J.-G. *ChemSusChem* **2008**, *1*, 676.
(3) Bruce, P. G.; Scrosati, B.; Tarascon, J.-M. *Angew. Chem., Int. Ed.* **2008**, *47*, 2930.
(4) Ji, L.; Lin, Z.; Alcoutlabi, M.; Zhang, X. *Energy Environ. Sci.* **2011**, *4*, 2682.
(5) Lee, S. W.; Gallant, B. M.; Byon, H. R.; Hammond, P. T.; Shao-Horn, Y. *Energy Environ. Sci.* **2011**, *4*, 1972.
(6) Wang, Y.; Li, H.; He, P.; Hosono, E.; Zhou, H. *Nanoscale* **2010**, *2*, 1294.
(7) Ji, L.; Rao, M.; Zheng, H.; Zhang, L.; Li, Y.; Duan, W.; Guo, J.; Cairns, E. J.; Zhang, Y. *J. Am. Chem. Soc.* **2011**, *133*, 18522.
(8) Guo, C. X.; Shen, Y. Q.; Dong, Z. L.; Chen, X. D.; Lou, X. W.; Li, C. M. *Energy Environ. Sci.* **2012**, DOI: 10.1039/C2EE21320F.
(9) Guo, C. X.; Wang, M.; Chen, T.; Lou, X. W.; Li, C. M. *Adv. Energy Mater.* **2011**, *1*, 736.
(10) Ji, L.; Zheng, H.; Ismach, A.; Tan, Z.; Xun, S.; Lin, E.; Battaglia, V.; Srinivasan, V.; Zhang, Y. *Nano Energy* **2012**, *1*, 164.
(11) Ji, L.; Tan, Z.; Kuykendall, T.; An, E. J.; Fu, Y.; Battaglia, V.; Zhang, Y. *Energy Environ. Sci.* **2011**, *4*, 3611.
(12) Candelaria, S. L.; Shao, Y.; Zhou, W.; Li, X.; Xiao, J.; Zhang, J.; Zhang, J.; Wang, Y.; Liu, J.; Li, J.; Cao, G. *Nano Energy* **2012**, *1*, 195.
(13) Liu, X.; Hu, Y.-S.; Müller, J.-O.; Schlögl, R.; Maier, J.; Su, D. S. *ChemSusChem* **2010**, *3*, 261.
(14) Ji, L.; Tan, Z.; Kuykendall, T. R.; Aloni, S.; Xun, S.; Lin, E.; Battaglia, V.; Zhang, Y. *Phys. Chem. Chem. Phys.* **2011**, *13*, 7170.
(15) Zhang, W.-M.; Wu, X.-L.; Hu, J.-S.; Guo, Y.-G.; Wan, L.-J. *Adv. Funct. Mater.* **2008**, *18*, 3941.
(16) Wu, Z.-S.; Zhou, G.; Yin, L.-C.; Ren, W.; Li, F.; Cheng, H.-M. *Nano Energy* **2012**, *1*, 107.
(17) Wang, D.; Choi, D.; Li, J.; Yang, Z.; Nie, Z.; Kou, R.; Hu, D.; Wang, C.; Saraf, L. V.; Zhang, J.; Aksay, I. A.; Liu, J. *ACS Nano* **2009**, *3*, 907.
(18) Chen, J. S.; Zhu, T.; Yang, X. H.; Yang, H. G.; Lou, X. W. *J. Am. Chem. Soc.* **2010**, *132*, 13162.
(19) Cheng, F.; Huang, K.; Liu, S.; Liu, J.; Deng, R. *Electrochim. Acta* **2011**, *56*, 5593.
(20) He, Y.; Huang, L.; Cai, J.-S.; Zheng, X.-M.; Sun, S.-G. *Electrochim. Acta* **2010**, *55*, 1140.
(21) Zhao, X.; Xia, D.; Zheng, K. *ACS Appl. Mater. Interfaces* **2012**, *4*, 1350.
(22) Yuan, S. M.; Li, J. X.; Yang, L. T.; Su, L. W.; Liu, L.; Zhou, Z. *ACS Appl. Mater. Interfaces* **2011**, *3*, 705.
(23) Cabana, J.; Monconduit, L.; Larcher, D.; Palacín, M. R. *Adv. Mater.* **2010**, *22*, E170.
(24) Jiao, F.; Bao, J.; Bruce, P. G. *Electrochem. Solid-State Lett.* **2007**, *10*, A264.
(25) Reddy, M. V.; Yu, T.; Sow, C. H.; Shen, Z. X.; Lim, C. T.; Subba Rao, G. V.; Chowdari, B. V. R. *Adv. Funct. Mater.* **2007**, *17*, 2792.
(26) Wang, B.; Chen, J. S.; Wu, H. B.; Wang, Z.; Lou, X. W. *J. Am. Chem. Soc.* **2011**, *133*, 17146.
(27) Kim, H. S.; Piao, Y.; Kang, S. H.; Hyeon, T.; Sung, Y.-E. *Electrochem. Commun.* **2010**, *12*, 382.
(28) Liu, Z.; Tay, S. W. *Mater. Lett.* **2012**, *72*, 74.
(29) Zhu, T.; Chen, J. S.; Lou, X. W. *J. Phys. Chem. C* **2011**, *115*, 9814.
(30) Cavaliere, S.; Subianto, S.; Savych, I.; Jones, D. J.; Roziere, J. *Energy Environ. Sci.* **2011**, *4*, 4761.
(31) Thavasi, V.; Singh, G.; Ramakrishna, S. *Energy Environ. Sci.* **2008**, *1*, 205.
(32) Dong, Z.; Kennedy, S. J.; Wu, Y. *J. Power Sources* **2011**, *196*, 4886.
(33) Ji, L.; Lin, Z.; Alcoutlabi, M.; Toprakci, O.; Yao, Y.; Xu, G.; Li, S.; Zhang, X. *RSC Adv.* **2012**, *2*, 192.
(34) Ji, L.; Medford, A. J.; Zhang, X. *J. Mater. Chem.* **2009**, *19*, 5593.
(35) Kim, C.; Yang, K. S.; Kojima, M.; Yoshida, K.; Kim, Y. J.; Kim, Y. A.; Endo, M. *Adv. Funct. Mater.* **2006**, *16*, 2393.
(36) Toprakci, O.; Ji, L.; Lin, Z.; Toprakci, H. A. K.; Zhang, X. *J. Power Sources* **2011**, *196*, 7692.
(37) Faridi-Majidi, R.; Sharifi-Sanjani, N. *J. Appl. Polym. Sci.* **2007**, *105*, 1351.
(38) McIntyre, N. S.; Zetaruk, D. G. *Anal. Chem.* **1977**, *49*, 1521.
(39) Temesghen, W. T.; Sherwood, P. S. *Anal. Bioanal. Chem.* **2002**, *373*, 601.
(40) Asami, K.; Hashimoto, K.; Shimodaira, S. *Corros. Sci.* **1976**, *16*, 35.
(41) Fujii, T.; de Groot, F. M. F.; Sawatzky, G. A.; Voogt, F. C.; Hibma, T.; Okada, K. *Phys. Rev. B* **1999**, *59*, 3195.
(42) Cherian, C. T.; Jayaraman, S.; M.V, R. V.; Sow, C. H.; B.V.R, C. *J. Mater. Chem.* **2012**, DOI: 10.1039/C2JM31053H.
(43) NuLi, Y.; Zhang, P.; Guo, Z.; Liu, H. *J. Electrochem. Soc.* **2008**, *155*, A196.
(44) Larcher, D.; Masquelier, C.; Bonnin, D.; Chabre, Y.; Masson, V.; Leriche, J. B.; Tarascon, J. M. *J. Electrochem. Soc.* **2003**, *150*, A133.
(45) Larcher, D.; Bonnin, D.; Cortes, R.; Rivals, I.; Personnaz, L.; Tarascon, J. M. *J. Electrochem. Soc.* **2003**, *150*, A1643.
(46) Morales, J.; Sanchez, L.; Martin, F.; Berry, F.; Ren, X. *J. Electrochem. Soc.* **2005**, *152*, A1748.
(47) Xu, K. *Energies* **2010**, *3*, 135.
(48) Liu, H.; Wang, G.; Park, J.; Wang, J.; Liu, H.; Zhang, C. *Electrochim. Acta* **2009**, *54*, 1733.
(49) Laruelle, S.; Grugeon, S.; Poizot, P.; Dolle, M.; Dupont, L.; Tarascon, J. M. *J. Electrochem. Soc.* **2002**, *149*, A627.
(50) Hosono, E.; Fujihara, S.; Honma, I.; Ichihara, M.; Zhou, H. *J. Electrochem. Soc.* **2006**, *153*, A1273.